optica

Explaining relative spectral red shifts in InGaN/GaN micropillars

W. Y. Fu (ID) **AND H. W. Choi***

Department of Electrical and Electronic Engineering, University of Hong Kong, Hong Kong, China
Corresponding author: hwchoi@hku.hk

There is common agreement that dimensional downscaling of III-nitride light-emitting diodes leads to spectral blue shifts due to strain relaxation of the quantum wells (QWs). Near-field photoluminescence (nf-PL) mapping of micropillars with InGaN/GaN QWs of different indium compositions using scanning near-field optical spectroscopy reveals that the nf-PL spectrum blue-shifts at the edge of a micropillar with respect to the center for QWs with a high indium composition, whereas a *relative* red shift is observed for QWs with a low indium composition. This observation suggests that the strain relaxation mechanism in micropillars is dependent on the indium composition, evident from changes in lattice parameters determined from calibrated diffraction patterns obtained by transmission electron microscopy. As indicated by molecular dynamics simulations, the strain of a micropillar is influenced by competing strain relaxation mechanisms between the lattice mismatch strain from the QWs, and residual strain from other layers and their interactions with the edge of the micropillar. First-principle calculations of GaN/InGaN/GaN heterostructures confirmed the effect of strain relaxation on the potential profiles, and, thus, on the spectral shifts from the micropillars. The findings of this work provide insight into strain-induced band profile engineering in optoelectronic devices built on lattice-mismatched systems.   © 2018 Optical Society of America under the terms of the OSA Open Access Publishing Agreement

OCIS codes: (130.3990) Micro-optical devices; (160.4760) Optical properties; (220.4000) Microstructure fabrication; (240.3990) Micro-optical devices; (230.5590) Quantum-well, -wire and -dot devices.

https://doi.org/10.1364/OPTICA.5.000765

1. INTRODUCTION

Quantum wells (QWs) are at the hearts of countless III-nitride light-emitting diodes (LEDs) that light up our modern world, providing electrical lighting solutions superior to their predecessors in many ways. Nonetheless, the LEDs in use today suffer from numerous drawbacks, including those associated with the quantum-confined Stark effect (QCSE). QCSE originates from the accumulation of spontaneous polarization charges at the well–barrier interface due to a lack of inversion symmetry in the wurtzite crystal structure, as well as strain-induced piezoelectric polarization charges arising from a lattice mismatch between the well–barrier materials. The polarization fields cause a deformation of the square well potential into a triangular potential profile, reducing the overlap between the electron and hole wavefunctions in the QWs, thus compromising the efficiencies of radiative recombinations. Emission wavelengths also become sensitive to the injection current, causing undesired spectral and color shifts due to carrier screening, especially for phosphor-pumped white-light LEDs. One of the solutions to overcome these issues is the growth or fabrication of non-planar quantum structures to replace the QWs. For instance, nanorod and nanowire LEDs have been demonstrated to improve internal quantum efficiencies [1,2] and light extraction efficiencies [3,4] compared with their planar counterparts.

The dimensions of the nanostructures can also be controlled for tuning of emission wavelengths [2,5–8]. All these enhancements are achieved by tuning of the bandgap or band profiles in the QWs.

Spectral shifting is one of the most prominent observations associated with dimensional downscaling, commonly attributed to the strain relaxation of the QWs [1,8–15]. There is general consensus that the atoms in the QWs will be displaced toward the edge to relax the strain induced by a lattice mismatch, thus resulting in a decrease in the piezoelectric polarization field and, thus, the QCSE [10,12], leading to a blue shift of the luminescent spectrum. However, with advancement of characterization techniques enabling spectroscopy with sub-diffraction spatial resolution, recent experimental observations on InGaN/GaN-based micro-/nanostructures have revealed inconsistent results. The report of Zhuang *et al.* [16] on a scanning electron microscopy-cathodoluminescence study of a low-indium-composition, single-QW nanorod shows a red shift at the edge of a QW from the cathodoluminescence spectra, which is inconsistent with the observations of spectral blue shifts at the edges of microstructures in earlier studies [9], explained qualitatively as an interplay between the QCSE and deformation potential (DP). This seems to suggest that there are multiple factors affecting the mechanism of strain-induced spectral shifts.

In view of such inconsistent observations, we report on a systematic study of optical emissions from etched micropillars, consisting of InGaN/GaN QWs of different indium compositions. Near-field photoluminescence (nf-PL) spectra from the micropillars were mapped with sub-diffraction spatial resolution by scanning near-field optical spectroscopy (SNOS) [13]. The strain profiles of the micropillars are simulated using the molecular dynamics technique, which can model the lattice-mismatched coherent interface and strain-relaxed surfaces more accurately than the conventional finite-element method (FEM) as used in previous studies [8,17]. In conjunction with structural characterization by transmission electron microscopy (TEM), molecular dynamics study of the strain relaxation mechanisms, and *ab initio* calculations of their effects on the potential profiles of QWs, the underlying mechanisms of the dimension-dependent spectral shifts, which are crucial for the development of novel strain-engineered devices, can be better understood.

2. RESULTS AND DISCUSSION

A. Experiments

Three *c*-plane InGaN/GaN QW samples with indium composition ranging from 11% to 18%, estimated using TEM energy-dispersive x-ray spectroscopy (EDX), are first patterned by microsphere lithography using 2 μm silica microspheres. A low concentration of the microsphere solution is used to ensure that each microsphere, or the fabricated micropillars, is spaced well apart for characterization purpose. This is followed by an inductively coupled plasma etch for 120 s with the microspheres as an etch mask, resulting in micropillars with a height of around 1 μm and a diameter of around 2 μm as observed by scanning electron microscopy (SEM) and TEM. The three fabricated micropillar samples have been labeled Bl, Cy, and Gn, which correspond to the colors of their photoluminescence (PL) emissions, namely, blue, cyan, and green, respectively. As determined from high-resolution TEM images, sample Bl has an ~240 nm thick p-GaN layer on top of eight periods of InGaN wells of ~5.2 nm thickness (10 atomic layers) and ~12.4 nm (24 atomic layers) thickness of GaN barriers. Samples Cy and Gn each have an ~560 nm thick *p*-GaN layer on top of 15 periods of InGaN wells of ~4.7 nm thickness (9 atomic layers) and ~13.5 nm (26 atomic layers) thickness of GaN barriers.

The micropillars are investigated using a SNOS nf-PL setup (based on a NT-MDT NTEGRA NSOM microscope) under an illumination-collection mode [18,19]. A coherent CUBE

405 nm continuous-wave diode laser source, operating at 60 mW of power, is coupled to a fiber, with the other end acting as an apertured tip for SNOS for the excitation of PL from the QWs of the micropillars, with a measured excitation power of ~0.1 mW. The nf-PL signal is then collected instantaneously by the same tip at the same position of excitation and passed to a Princeton Instrument Acton SP2150i spectrometer with a 1200 g/mm grating. The spatial resolution of the mapping depends on the diameter of the aperture, which is about 70 nm, and the distance of the QWs in the samples from the tip, as the FWHM of the excitation and collection profiles, which resembles an Airy distribution, expands accordingly from about 200 to 400 nm.

As the peak wavelengths extracted from the spectra by Gaussian fitting fluctuate possibly due to fluctuations in local indium content, the *relative* spectral shift with respect to the distance from the centers of the micropillars is plotted for statistical analysis in Fig. 1, which shows the different *relative* spectral shift behavior for the samples. The *relative* spectral shift is defined as the difference in wavelengths between the measurement point and the center of a micropillar. It is interesting to see differing trends of spectral shifts between the three samples. Micropillar Bl exhibits an increasing *relative* spectral red shift beginning from ~0.5 μm away from the center as shown in Fig. 1(a), whereas micropillar Gn experiences *relative* blue shifts near the edge with respect to the center as shown in Fig. 1(c), in line with the prediction of Wu *et al.* [9] who suggested that strain relaxation ("dilation") occurs at the edges of the QWs, and thus the term "edge effect". The *relative* spectral shifts of micropillar Cy, which has indium composition between those of micropillars Bl and Gn in the wells, appear to be negligible, as illustrated in Fig. 1(b). Note that the strongest *relative* spectral shift is observed when the probe is positioned slightly beyond the edge of the micropillar, whereby coupling between the probe and sidewall emission is dominated by emission from the edge of the pillar, as signals from the center are unlikely to be collected. This implies that the *relative* spectral blue shift for micropillar Bl is likely an "edge effect," contrary to micropillar Gn.
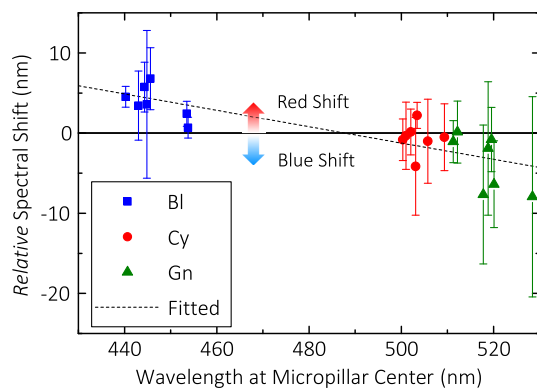
To ensure that this trend of indium-composition-dependent *relative* spectral shift is not an artifact caused by local fluctuations of indium content and defects, the nf-PL mappings have been repeated seven times for each sample—each time randomly picking a different micropillar. The emission wavelengths at the center and the edge, for calculating the *relative* spectral shift between the
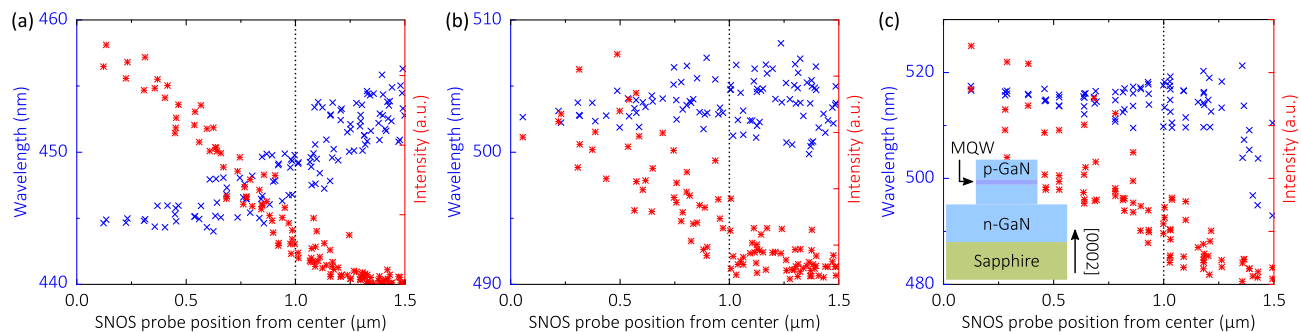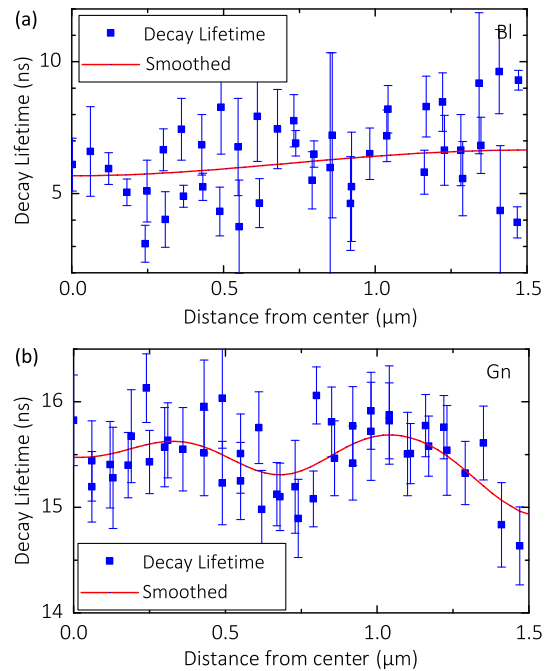

Fig. 1. SNOS measurement results of micropillars of 2 μm diameter and 1 μm height, on (a) sample Bl (blue emission), (b) sample Cy (cyan emission), and (c) sample Gn (green emission), showing the corresponding plot of nf-PL peak wavelengths and peak intensity w.r.t. the SNOS probe position from the center of the micropillars. The black dotted line at 1 μm corresponds to the edge of a micropillar. The inset on the bottom left in (c) shows a schematic diagram of the micropillar structure.

center and the edge, are taken as the averaged wavelengths in the circular region of $r \leq 0.25$ μm and the annular region of 1.25 μm $\leq r \leq 1.5$ μm, respectively, where r is the probe position with respect to the center of the micropillar. As shown in Fig. 2, the trend of *relative* spectral shift is fairly obvious—as the indium composition increases, the *relative* spectral shift changes from a red shift to a blue shift. Subsequently, the discussion will be focused on micropillars Bl and Gn, which exhibited large contrasts in *relative* spectral shifts due to their difference in indium compositions.

Micropillars Bl and Gn are further investigated using a Picoquant time-correlated single photon counting (TCSPC) setup coupled to the SNOS. A 405 nm picosecond pulsed laser source, Picoquant LDH-405, is coupled to the SNOS fiber tip to excite the sample at a repetition rate of 10 MHz. The collected nf-PL signals are then received by an MPD PDM single photon avalanche diode detector. A PicoHarp 300 TCSPC module is then used to measure the time delay by comparing the timing of a received photon with that of the received electronic synchronization signal when the laser pulse was triggered. This time delay data are then accumulated to form a histogram that represents the lifetime of the nf-PL. As plotted in Fig. 3, the line profiles of near-field time-resolved PL (nf-TRPL) decay lifetimes have been measured. As the proportion of non-radiative lifetime should stay relatively constant throughout the micropillar, since there should be little to no change in the spatial distribution of defect density, the trend of the decay can be inferred to be caused by a change in the radiative lifetime. A lengthening of the decay lifetime with increasing distance from the center is observed for micropillar Bl, which also exhibits increasing *relative* spectral red shifts from the center toward the edge as shown in Fig. 1(a). On the other hand, the decay lifetime for micropillar Gn drops abruptly near the edge, consistent with the trend of *relative* spectral blue shifts in Fig. 1(c). Variations of the electron–hole wavefunction overlap would lead to changes in the oscillator strength, which is inversely proportional to the PL decay lifetime. Hence, a reduction in electron–hole wavefunction overlap together with a decrease in the QW bandgap for micropillar Bl, and vice versa for micropillar Gn, implies that the band profiles have been changed, which is likely to be caused by a modified extent of the QCSE.

Fig. 3. nf-TRPL measurement results of micropillars (a) Bl and (b) Gn, of 2 μm diameter and 1 μm height, showing the corresponding plot of nf-TRPL decay lifetime w.r.t. distance from the center of the micropillars.

Micro-PL (μ-PL) measurements for micropillars Bl and Gn have been undertaken to compare the emission characteristics at the microscopic regime with the SNOS measurements. A 349 nm diode-pumped solid-state pulsed laser, with a pulse width of 4 ns, a repetition rate of 1 kHz, and average power of about 10 mW, is used for μ-PL excitation. As shown in Fig. 4, both micropillars exhibit spectral blue shifts when compared with their as-grown counterparts, consistent with results from previous studies [1,8–15] that the fabrication of micropillars causes a spectral blue shift due to strain relaxation. Combining this observation with the opposite trends demonstrated in their *relative* nf-PL spectral shift behavior in Fig. 1 and 2, it can be implied that the μ-PL spectral blue shift observed for micropillar Bl, which also exhibits a *relative* nf-PL spectral red shift at the edge, might actually be due to a spectral blue shift at the central region of the micropillar rather than toward the edge. Moreover, the peak emission wavelength for micropillar Bl red-shifts with increasing temperature, whereas that for micropillar Gn is nearly independent on temperature, as illustrated in Fig. 4; this may be attributed to carrier localization due to the higher indium content in micropillar Gn.

The strain states of the micropillars are then investigated using calibrated diffraction patterns obtained with an FEI Tecnai G2 20 transmission electron microscope (Fig. 5) using the atomic plane spacings $d_{1\bar{1}00}$ and d_{0002}. Bright-field images and diffraction patterns are then obtained along the $11\bar{2}0$ zone axis of the cross-sectional TEM specimens of the micropillars, as shown in Fig. 5. To estimate the relative strain states of the samples, lattice parameters were extracted from calibrated diffraction patterns obtained via a selective area aperture of ~50 nm diameter by using the measured spacings d of the 0002 and 01$\bar{1}$0 spots from the 0000 spot in the equation (for a wurtzite structure)
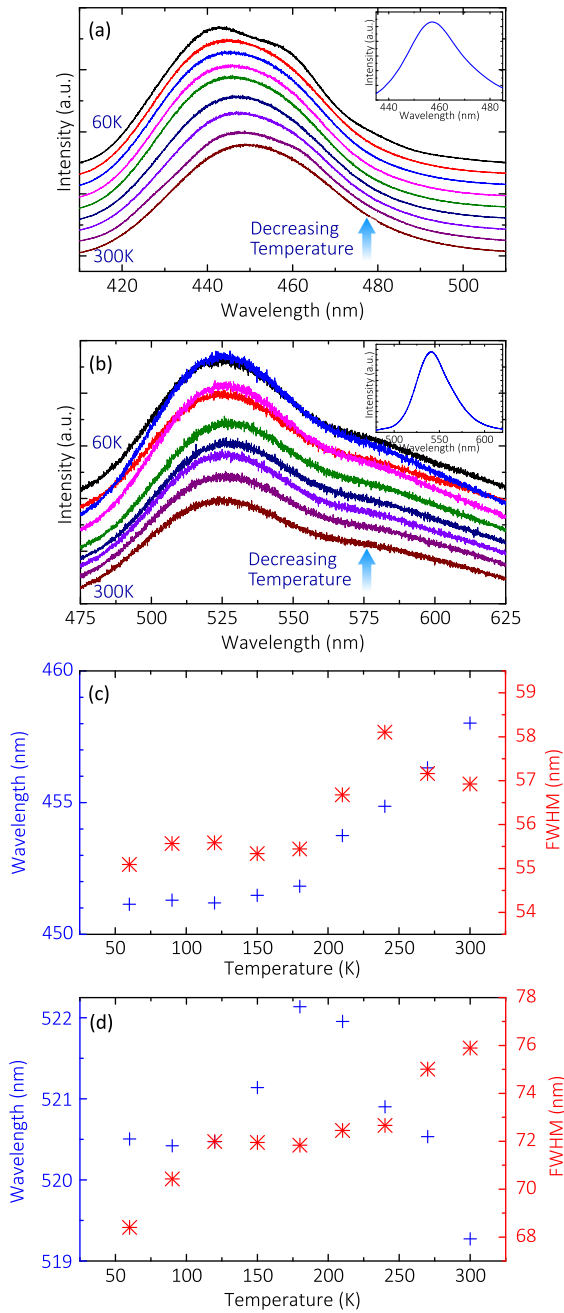

Fig. 2. SNOS measurements of nf-PL from micropillars on samples Bl, Cy, and Gn. nf-PL spectra maps were collected using SNOS from randomly picked micropillars on each sample. The *relative* spectral shift in this figure is the difference between the averaged peak wavelength at the center and at the edge from a PL map. The trend of *relative* spectral shift is shown by a fitted line (dashed line). The error bar indicates the total spread of peak emission wavelengths at the center and at the edge.

Fig. 4. Temperature-dependent μ-PL results of micropillars (a) Bl and (b) Gn, of 2 μm diameter and 1 μm height. The insets show the μ-PL of the corresponding as-grown samples. Panels (c) and (d) show the results of fitting a Gaussian to the data from (a) and (b), respectively. Note that the Fabry–Perot fringes in the PL spectra have been removed by FFT filtering.

$$\frac{1}{d_{hkil}} = \sqrt{\frac{a^2}{h^2} + \frac{3a^2}{(h+2k^2)^2} + \frac{c^2}{l^2}}, \qquad (1)$$

where a and c are the lattice parameters for the diffraction spot *hkil*. The center position of a diffraction spot is estimated by fitting with a 2D Gaussian function for sub-pixel accuracy. Since the systematic errors inherited from the process of diffraction pattern calibration could be relatively large as compared with the effect of strain on the calculated lattice parameters, only the relative
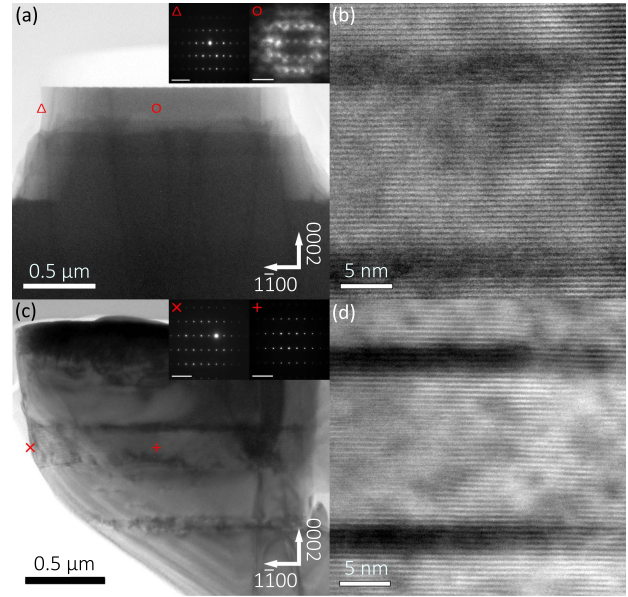
Fig. 5. Cross-sectional bright-field TEM images and (inset) selective area diffraction patterns obtained along the $11\bar{2}0$ zone axis of micropillars (a) Bl and (c) Gn. Panels (b) and (d) show the corresponding high-resolution TEM images of the QWs of Bl and Gn, respectively, and (inset) the SEM images of micropillars from the corresponding samples for reference. The white lines in the insets correspond to a length of 5 nm^{-1} for the diffraction patterns and 1 μm for the SEM images.

changes in lattice spacings between the edge and the center of the micropillars are compared.

As the atomic plane spacings from $\{1\bar{1}00\}$ and $\{0002\}$ are directly related to the lattice parameters a and c by a factor of $2/\sqrt{3}$ and 2, respectively, as described by Eq. (1), the change in lattice parameters along these two directions can be deduced. As shown in Table 1, both micropillars show an increase in the in-plane lattice parameter along the $[1\bar{1}00]$ direction at the edge relative to the center, with similar rates of change, indicating a reduction in the in-plane compressive strain at the edge, as predicted by previous studies [9,10]. However, both micropillars also show an increase in the atomic spacing along the [0002] direction, which suggests that the edge may be tensile-strained along the out-of-plane direction. Given that the change in volume under elastic deformation is negligible, the in-plane lattice parameter is compressively strained along the $[11\bar{2}0]$ direction, i.e., the direction perpendicular to the TEM specimen, as illustrated by the estimated values in Table 1 by assuming the lattice parameter a at the center of the micropillar is the same along both $[1\bar{1}00]$ and $[11\bar{2}0]$ directions. Since both micropillars have the same diameter, the increase in out-of-plane tensile strain at the edge of micropillar Bl can be attributed to a difference in indium composition. This difference in out-of-plane strain, and also the compressive strain along the $[11\bar{2}0]$ direction, is the fundamental cause of the opposite trends in *relative* nf-PL spectral shift between the two samples. Since the InGaN alloys are bound to introduce a lattice mismatch strain into the GaN barrier layers in the QWs, and that the μ-PL spectra exhibit blue shifts at the macroscopic scale, confirming strain relaxation in both samples, it can be deduced that an additional strain relaxation mechanism that is dependent on indium composition is causing the increase in the out-of-plane

Table 1. Lattice Parameters Extracted from the 0002 and 1$\bar{1}$00 Spots of the Calibrated Selective Area Diffraction Images in Fig. 5

Micropillars	$\frac{2}{\sqrt{3}}d_{1\bar{1}00}^{center}$ (Å)	$\frac{2}{\sqrt{3}}d_{1\bar{1}00}^{edge}$ (Å)	$2d_{0002}^{center}$ (Å)	$2d_{0002}^{edge}$ (Å)	Change along [1$\bar{1}$00]	Change in Out–of–Plane Lattice	Estimated Change along [11$\bar{2}$0]
Bl	3.28780	3.29686	5.23081	5.28048	−0.275%	−0.941%	1.228%
Gn	3.23560	3.24468	5.25028	5.27437	−0.280%	−0.457%	0.741%

tensile strain. Since the change in the in-plane lattice is no longer homogeneous in all directions, due to micropillar fabrication, the following discussion on spectral shift will mainly focus on the change in the out-of-plane lattice, which reflects the net effect of the in-plane lattice distortion in all directions and is still directly related to the spectral shift.
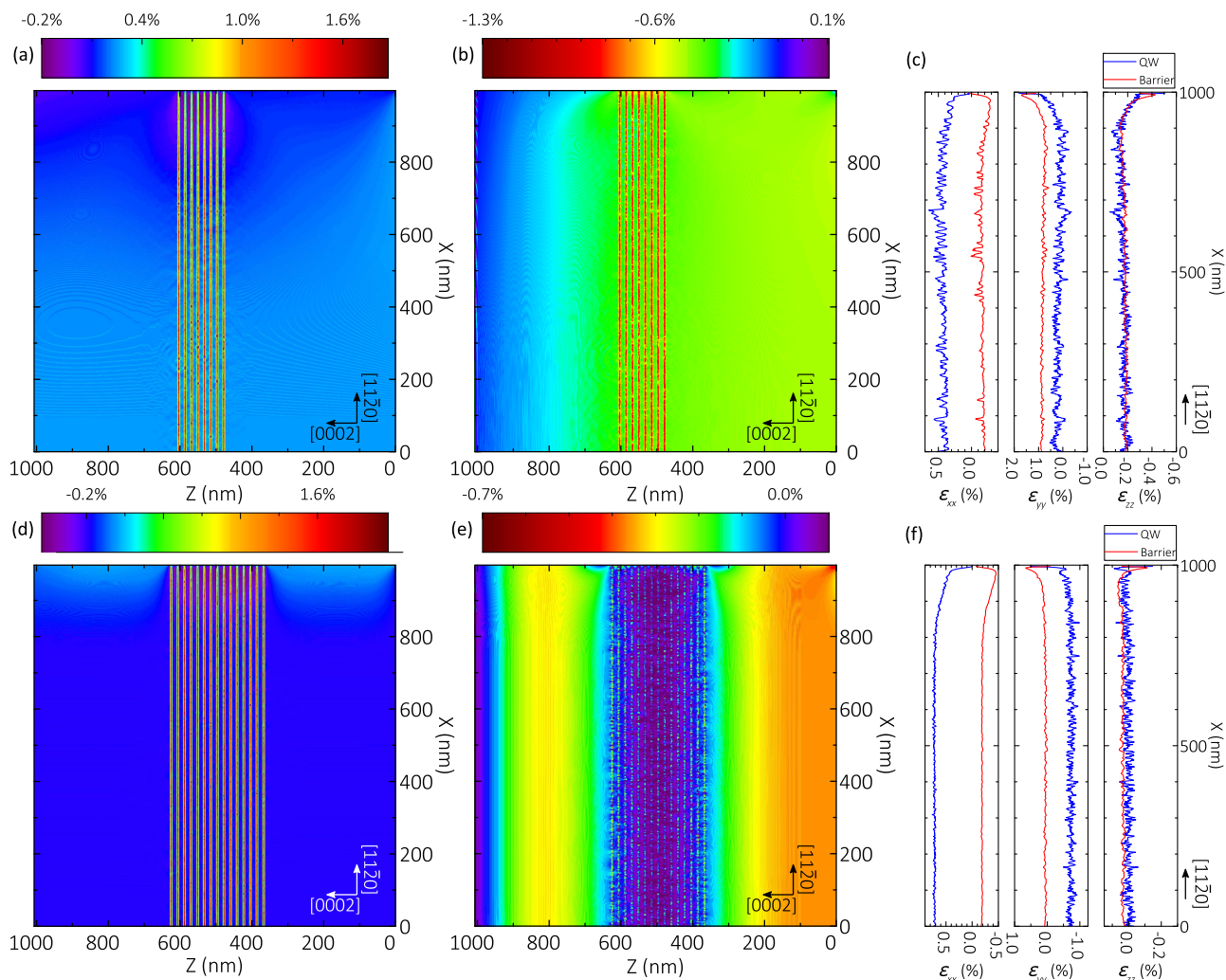
B. Simulations

The strain relaxation mechanisms of the micropillars are thus investigated using molecular dynamics simulations by LAMMPS [20] with a Stillinger–Weber potential [21] for InGaN [22,23]. 2D simulations of a micropillar with a diameter of 2 μm are set up with a *c*-plane wurtzite GaN block. The crystal structure is set up such that *x* axis is along the [11$\bar{2}$0] direction and *z* axis is along the [0002] direction. The computational domain is reduced to half the micropillar, i.e., a dimension of 1 μm × 1 μm, by imposing a symmetric boundary, which restricts the lateral movement of the atoms, on one side of the block. The GaN block is fixed at the bottom ($y = 0$) with a compressive strain of 0.023% to emulate the situation that the micropillar is situated on a partially relaxed GaN buffer with a biaxial stress of 1 GPa. The values of QW layer thicknesses and indium content are estimated from cross-sectional TEM images and EDX results, respectively, to simulate the QW structure of samples Bl and Gn. The p-GaN layer thickness is assigned a value that is the average of both samples, i.e., ∼400 nm, for the purpose of comparison. The InGaN layers are initialized to be lattice-matched to the GaN layers, i.e., having coherent interfaces, and are implemented as a random alloy, i.e., the Ga atoms in the wurtzite structure are randomly replaced with In atoms within the supposed InGaN QW regions, with the proportion of In atoms satisfying the estimated indium content for the QWs. The structure is then subjected to an energy minimization to relax the atomic positions. For sample Bl, eight pairs of InGaN/GaN QWs are implemented, with thicknesses of ∼5.2 nm (10 atomic layers) of the InGaN wells with 11% indium content, and ∼12.4 nm (24 atomic layers) thickness of GaN barriers. Similarly, 15 pairs of QWs of sample Gn have InGaN wells with 18% indium content and ∼4.7 nm (9 atomic layers) thickness, and GaN barriers with a thickness of ∼13.5 nm (26 atomic layers).

The strain maps in Fig. 6 are calculated from the relaxed atomic positions after the minimization converged. The lattice spacings of the atoms are extracted around predefined grid points. The spatially averaged strain can then be calculated by comparing the extracted lattice parameters with the fully relaxed lattice parameters. The relaxed lattice parameters are obtained from the InGaN Stillinger–Weber potential [22,23], for both GaN ($a = 3.187$Å and $c = 5.201$Å) and InN ($a = 3.521$Å and $c = 5.746$Å), in good agreement with experimental observations [24]. The parameters for InGaN can thus be obtained using Vegard's law. The results show that the strain field at the edge

is fairly different for the two simulations with different indium compositions. As can be seen in Fig. 6, both micropillars exhibit a relaxation of the QWs at the edge regions, as expected. However, a significant increase of out-of-plane strain is observed at the edge of micropillar Bl (starting from $X = 900$ nm), consistent with the lattice parameters determined from TEM as listed in Table 1. This increase of strain originates from the relaxation of the residual strain from the non-fully relaxed GaN buffer layer. This residual strain is induced from the lattice mismatch between the GaN film and the sapphire substrate, as well as a thermal mismatch between the QWs and the low-temperature-grown GaN buffer layer. When the micropillar relaxes as a whole, the lattice will try to maintain coherence at the base of the micropillar, thus increasing the out-of-plane tensile strain at the edge, as shown in Fig. 6(c). This second mechanism is only revealed for the QWs with low indium content, whereby relaxation of the strain caused by the InGaN/GaN lattice mismatch is weak (diminishes). With increase in indium composition, the strain due to lattice mismatch strain is increases, giving rise to a larger decrease in the in-plane compressive strain at the edge due to strain relaxation, and, thus, an increase in the out-of-plane compressive strain to oppose a change in lattice volume. This increase in the out-of-plane compressive strain would have counteracted the out-of-plane tensile strain introduced by the second mechanism. It is also observed that there is an abrupt increase in the out-of-plane strain within a 10 nm region from the edge in both samples, consistent with the calculations of Böcklin *et al.* [10] showing a tensile-strained annulus near the edge due to the in-plane relaxation of the QW layer. Note that the numerical fluctuations of the curves are due to the random distribution of indium atoms in the InGaN alloy in the simulations, unlike the assumption of InGaN as a homogenous elastic material using the FEM.

Although the directions of the *relative* spectral shifts are different, both mechanisms are essentially "edge effects". In both samples, the QWs relax at the edge, similarly to the calculations of in-plane strain by the FEM in previous studies [8,17]. However, micropillar Bl has an increased out-of-plane strain at the edge due to edge bounding. As shown in Fig. 6, changes to the strain fields occur mainly within ∼100 nm from the edge of a micropillar. By reducing the diameter of a micropillar, the ratio of the "edge region" to the "center region" increases, thus allowing PL wavelengths to be adjusted according to dimensions [5].

As *c*-plane (polar) wurtzite III-nitride crystals suffer from a strong QCSE, the piezoelectric polarization field will respond to a change of strain, altering the electric potential profile and thus the bandgap energies of the QWs [25]. Although there have been studies on the effect of in-plane strain in InGaN/GaN QWs on their emission characteristics [9,25], the effect of out-of-plane strain in QWs, on which the second strain relaxation mechanism is dependent, is the focus of this work. To study the impact of strain relaxation mechanisms on the emission wavelength, the
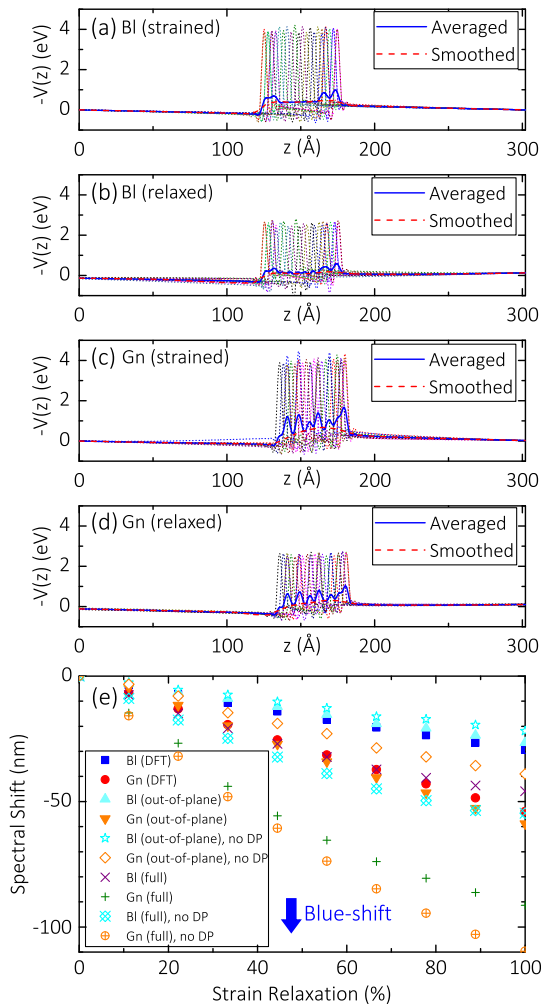
Fig. 6. Strain fields calculated from relaxed atomic positions simulated by molecular dynamics simulations. The center and the edge of the simulated micropillars are at $X = 0$ nm and $X = 1000$ nm, respectively. (a) In-plane strain and (b) out-of-plane strain of micropillar Bl, and (d) in-plane strain and (e) out-of-plane strain of micropillar Gn. Panels (c) and (f) show the averaged strain profiles, ϵ_{xx}, ϵ_{yy}, and ϵ_{zz}, of the QWs and barriers in micropillars Bl and Gn, respectively.

bandgap energies and electric potential profiles of the GaN/InGaN/GaN heterostructures are calculated, respectively, by solving the Schrödinger equation using the $\mathbf{k} \cdot \mathbf{p}$ perturbation theory [25–27] and the first-principle density functional theory (DFT) calculations using Siesta [28] with a Perdew–Burke–Ernzerhof exchange-correlation functional [29]. Troullier–Martins [30] norm-conserving pseudopotentials are generated using the ATOM program, with semicore d electrons explicitly included in the valence electron sets for Ga and In atoms. Double-ζ polarized basis sets are used. The InGaN layers of the heterostructures are constructed according to the multiple quantum wells (MQW) structures of samples Bl and Gn used in the above molecular dynamics studies, but using only one unit cell in the in-plane direction, that is, an atomic column with periodic boundary conditions in all three dimensions. The DFT simulations are repeated multiple times with different indium site configurations, which are assigned quasi-randomly in the InGaN alloy, of the same indium composition to simulate the macroscopic potential profiles of the samples. Each of these simulations is repeated for its strained state (with atomic coordinates corresponding to a relaxed

wurtzite GaN lattice) and relaxed state (with atomic coordinates relaxed in the out-of-plane direction in a molecular dynamics simulation). The potential profile resulting from each DFT simulation is shown in Figs. 7(a)–7(d).

Even though the lattice parameter is kept constant in the in-plane direction during the DFT simulations, the potential energies in the InGaN layer of both micropillars decrease after out-of-plane relaxation. This implies that the effect caused by QCSE decreases with relaxation of the InGaN layer. Figure 7(e) shows the emission wavelengths calculated from $\mathbf{k} \cdot \mathbf{p}$ calculations using the averaged potential profiles estimated from the DFT simulations shown in Figs. 7(a)–7(d) and plotted against the ratio of strain relaxation. The DFT potential profiles are linearly interpolated when calculating the intermediate points, and the results following conventional $\mathbf{k} \cdot \mathbf{p}$ calculations [25–27] are plotted as reference in Fig. 7(e). The results show that conventional $\mathbf{k} \cdot \mathbf{p}$ calculations, taking into account the effect of DP [25], closely match those using DFT potential profiles. Note that, according to the calculations, a shift in the conduction band energy level as a result of strain relaxation is the major contribution toward the
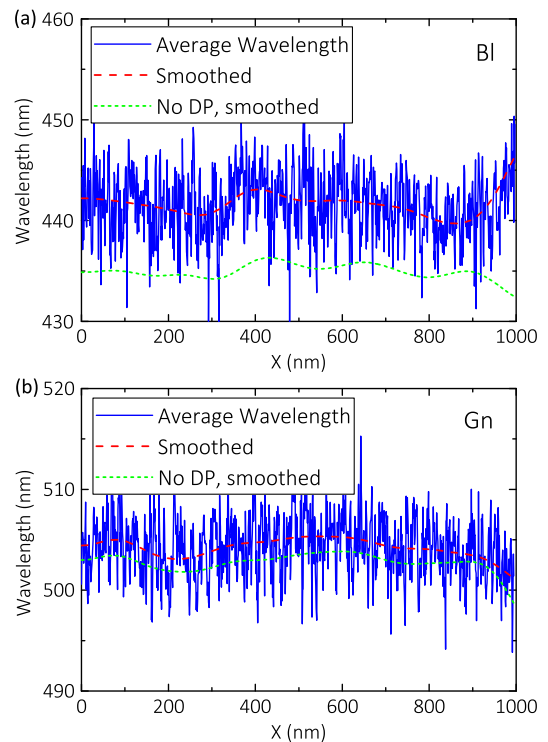
spectral shifts (see Supplement 1). When the micropillars are subjected to out-of-plane relaxation, the emission wavelengths can shift by up to ~30 nm and ~50 nm, respectively, for micropillars Bl and Gn. However, the emission wavelength of a fully relaxed InGaN layer, including in-plane relaxation, could have shifted by ~45 nm and ~90 nm, respectively, for micropillars Bl and Gn, according to conventional $\mathbf{k} \cdot \mathbf{p}$ calculations. Moreover, the contributions from DP differ for out-of-plane relaxation and full strain relaxation. Here in Fig. 7(e), results without DP (by setting the values of DPs [25] to 0) are also shown for comparison purpose. By comparing the curves "Bl (out-of-plane)" and "Bl (out-of-plane) no DP" in Fig. 7(e), which represent,

respectively, the spectral shift induced in the micropillar Bl by relaxation of out-of-plane tensile strain with and without the effect of DP, it is obvious that the rate of change of blue shift with respect to strain relaxation increases when the effect of DP is included. In contrast, for the case of full strain relaxation, the effect of DP reduces the rate of change of blue shift with respect to strain relaxation, as observed by comparing the curves "Bl (full)" and "Bl (full), no DP". Micropillar Gn also exhibits similar trends as shown in Fig. 7(e). As the out-of-plane tensile strain would have increased the slope of the blue shift, this implies that the decrease in slope for the case of full strain relaxation is caused by a relaxation of the in-plane compressive strain. The opposite effects from DP can be explained by the fact that the out-of-plane strain and the in-plane strain are tensile and compressive, respectively. Therefore, when the out-of-plane strain becomes less relaxed, i.e., going from right to left in Fig. 7(e), the larger slope of the spectral shift in response to a change in strain will result in a higher red shift as compared with that without the contribution from the DP. This explains our observations of a *relative* nf-PL spectral red shift at the edge of micropillar Bl in Figs. 1 and 2, since it suffers from a higher out-of-plane strain state at the edge due to lower indium compositions, as demonstrated in Figs. 6(a)–6(c), but has a trend of in-plane compressive strain similar to that of micropillar Gn.

The calculated results illustrated in Fig. 7 assumed that the GaN layers are relaxed, except for the DFT potential profiles. Apparently, the strain fields determined from molecular dynamics simulations in Fig. 6 show that the GaN barrier layers in the QWs could have experienced out-of-plane strain as well. Since the GaN layers act as barriers in the band profile to the QWs, the effect of

Fig. 7. Averaged potential energy profiles (solid blue line) of the GaN/InGaN/GaN heterostructure calculated from *ab initio* calculations at the band edge for [(a), (b)] sample Bl and [(c), (d)] sample Gn. The dotted lines are the smoothed individual potential profiles with different indium distributions calculated from DFT simulations before averaging. (e) Peak emission wavelengths w.r.t. strain relaxation, comparing the results calculated using the potential profiles in (a)–(d) ["Bl (DFT)" and "Gn (DFT)"] with conventional $\mathbf{k} \cdot \mathbf{p}$ calculations, both under out-of-plane strain relaxation, with ["Bl (out-of-plane)" and "Gn (out-of-plane)"] and without the effect of DP ["Bl (out-of-plane), no DP" and "Gn (out-of-plane), no DP"]. Calculation results with full (in-plane and out-of-plane) strain relaxation are shown as reference ["Bn (full)"; "Gn (full)"; "Bn (full), no DP"; "Gn (full), no DP"]. Note that the negative sign indicates a blue shift.

Fig. 8. Peak emission wavelengths calculated for micropillars (a) Bl and (b) Gn, using simulated strain fields obtained from the molecular dynamics simulations shown in Fig. 6. For reference purpose, calculation results without the effect of DP (green short-dash line) are also shown.

strain in the GaN layers should typically be opposite that of the InGaN well layer. To take into account this effect, the values of the strain fields, which include strain from all layers calculated from molecular dynamics simulations, are inserted into the Schrödinger equation for calculation of emission wavelengths. For each point of calculation, a locally averaged indium composition is also used instead of using a single value of indium composition for all positions in all QWs. Also, to maintain the traction-free boundary condition such that the stress $\tau_{zz} = 0$, a modified in-plane strain term is used:

$$\epsilon'_\perp = -\epsilon_\perp - \frac{C_{33}}{C_{13}}\epsilon_{zz}. \tag{2}$$

The calculated averaged emission wavelengths over all QWs weighted by the electron–hole wavefunction overlap integral are shown in Fig. 8. Micropillars Bl and Gn show, respectively, a *relative* red shift and a blue shift at the edge as expected from our observations and discussions so far. However, by excluding the contribution from the DP, the red shift in micropillar Bl is no longer present. This validates the claim of Zhuang *et al.* [16] on the interplay of DP and QCSE. However, if the strain profile from Gn with a deliberately decreased indium composition is used in the calculation of the emission wavelength profile, no red shift is observed at the edge. This means that the red shift phenomenon at the edge is contributed by an increase in out-of-plane strain and the effect of DP.

3. CONCLUSION

A systematic study of the nf-PL characteristics of InGaN/GaN micropillars with different indium compositions has been conducted by SNOS. The results show that the *relative* spectral shift of PL emission from the micropillars at the edge is dependent on the indium composition of the QWs. Lattice parameters deduced from calibrated TEM diffraction patterns verified the change in strain at the edge w.r.t. indium composition. A change in strain relaxation mechanism with the indium content of the QWs is then demonstrated using molecular dynamics simulations. DFT calculations comparing the potential profiles of strained and relaxed GaN/InGaN/GaN heterostructures concur with the experimental observations, that is, a strain-induced change in the QCSE and DP caused a shift in the bandgap energies of the QWs. The findings of this work provide insight into strain-induced band profile engineering in novel optoelectronic applications built on lattice-mismatched systems, especially for monolithically integrated optoelectronic platforms.

See Supplement 1 for supporting content.

REFERENCES

1. Q. Wang, J. Bai, Y. P. Gong, and T. Wang, "Influence of strain relaxation on the optical properties of InGaN/GaN multiple quantum well nanorods," J. Phys. D **44**, 395102 (2011).
2. C. Kolper, M. Sabathil, M. Mandl, M. Strassburg, and B. Witzigmann, "All-InGaN phosphorless white light emitting diodes: an efficiency estimation," J. Lightwave Technol. **30**, 2853–2862 (2012).
3. H. W. Choi, C. W. Jeon, M. D. Dawson, P. R. Edwards, R. W. Martin, and S. Tripathy, "Mechanism of enhanced light output efficiency in InGaN-based microlight emitting diodes," J. Appl. Phys. **93**, 5978–5982 (2003).
4. W. Li, K. Li, F.-M. Kong, Q.-Y. Yue, X.-L. Chen, and X.-J. Yu, "Study of light extraction efficiency of GaN-based light emitting diodes by using top micro/nanorod hybrid arrays," Opt. Quantum Electron. **46**, 1413–1423 (2014).
5. C. Feng, J.-A. Huang, and H. W. Choi, "Monolithic broadband InGaN light-emitting diode," ACS Photon. **3**, 1294–1300 (2016).
6. C. Hahn, Z. Zhang, A. Fu, C. H. Wu, Y. J. Hwang, D. J. Gargas, and P. Yang, "Epitaxial growth of InGaN nanowire arrays for light emitting diodes," ACS Nano **5**, 3970–3976 (2011).
7. Y.-J. Lu, H.-W. Lin, H.-Y. Chen, Y.-C. Yang, and S. Gwo, "Single InGaN nanodisk light emitting diodes as full-color subwavelength light sources," Appl. Phys. Lett. **98**, 233101 (2011).
8. Y. Kawakami, A. Kaneta, L. Su, Y. Zhu, K. Okamoto, M. Funato, A. Kikuchi, and K. Kishino, "Optical properties of InGaN/GaN nanopillars fabricated by postgrowth chemically assisted ion beam etching," J. Appl. Phys. **107**, 023522 (2010).
9. Y. R. Wu, C. H. Chiu, C. Y. Chang, P. C. Yu, and H. C. Kuo, "Size-dependent strain relaxation and optical characteristics of InGaN/GaN nanorod LEDs," IEEE J. Sel. Top. Quantum Electron. **15**, 1226–1233 (2009).
10. C. Böcklin, R. G. Veprek, S. Steiger, and B. Witzigmann, "Computational study of an InGaN/GaN nanocolumn light-emitting diode," Phys. Rev. B **81**, 155306 (2010).
11. J. Bai, Q. Wang, and T. Wang, "Characterization of InGaN-based nanorod light emitting diodes with different indium compositions," J. Appl. Phys. **111**, 113103 (2012).
12. C. H. Chang, L. Y. Chen, L. C. Huang, Y. T. Wang, T. C. Lu, and J. J. Huang, "Effects of strains and defects on the internal quantum efficiency of InGaN/GaN nanorod light emitting diodes," IEEE J. Quantum Electron. **48**, 551–556 (2012).
13. Y. Zhang, J.-A. Huang, K. H. Li, D. Bai, Y. Wang, T. Wang, and H. W. Choi, "Influence of strain on emission from GaN-on-Si microdisks," J. Phys. D **49**, 375103 (2016).
14. V. Ramesh, A. Kikuchi, K. Kishino, M. Funato, and Y. Kawakami, "Strain relaxation effect by nanotexturing InGaN/GaN multiple quantum well," J. Appl. Phys. **107**, 114303 (2010).
15. C. Rivera, U. Jahn, T. Flissikowski, J. L. Pau, E. Munoz, and H. T. Grahn, "Strain-confinement mechanism in mesoscopic quantum disks based on piezoelectric materials," Phys. Rev. B **75**, 045316 (2007).
16. Y. D. Zhuang, J. Bruckbauer, P. A. Shields, P. R. Edwards, R. W. Martin, and D. W. E. Allsopp, "Influence of stress on optical transitions in GaN nanorods containing a single InGaN/GaN quantum disk," J. Appl. Phys. **116**, 174305 (2014).
17. E. Y. Xie, Z. Z. Chen, P. R. Edwards, Z. Gong, N. Y. Liu, Y. B. Tao, Y. F. Zhang, Y. J. Chen, I. M. Watson, E. Gu, R. W. Martin, G. Y. Zhang, and M. D. Dawson, "Strain relaxation in InGaN/GaN micro-pillars evidenced by high resolution cathodoluminescence hyperspectral imaging," J. Appl. Phys. **112**, 013107 (2012).
18. T. Saiki and K. Matsuda, "Near-field optical fiber probe optimized for illumination collection hybrid mode operation," Appl. Phys. Lett. **74**, 2773–2775 (1999).
19. H. Nakamura, T. Sato, H. Kambe, K. Sawada, and T. Saiki, "Design and optimization of tapered structure of near-field fibre probe based on finite-difference time-domain simulation," J. Microsc. **202**, 50–52 (2001).
20. S. Plimpton, "Fast parallel algorithms for short-range molecular-dynamics," J. Comput. Phys. **117**, 1–19 (1995).
21. F. H. Stillinger and T. A. Weber, "Computer-simulation of local order in condensed phases of silicon," Phys. Rev. B **31**, 5262–5271 (1985).
22. A. Bere and A. Serra, "On the atomic structures, mobility and interactions of extended defects in GaN: dislocations, tilt and twin boundaries," Philos. Mag. **86**(15), 2159–2192 (2006).
23. H. P. Lei, J. Chen, S. Petit, R. Ruterana, X. Y. Jiang, and G. Nouet, "Stillinger–Weber parameters for In and N atoms," Superlattices Microstruct. **40**, 464–469 (2006).
24. I. Vurgaftman and J. R. Meyer, "Band parameters for nitrogen-containing semiconductors," J. Appl. Phys. **94**, 3675–3696 (2003).
25. Q. M. Yan, P. Rinke, A. Janotti, M. Scheffler, and C. G. Van de Walle, "Effects of strain on the band structure of group-III nitrides," Phys. Rev. B **90**, 125118 (2014).

26. A. Bonfiglio, M. Lomascolo, G. Traetta, R. Cingolani, A. Di Carlo, F. Della Sala, P. Lugli, A. Botchkarev, and H. Morkoc, "Well-width dependence of the ground level emission of GaN/AlGaN quantum wells," J. Appl. Phys. **87**, 2289–2292 (2000).

27. S. L. Chuang and C. S. Chang, "A band-structure model of strained quantum-well wurtzite semiconductors," Semicond. Sci. Technol. **12**, 252–263 (1997).

28. J. M. Soler, E. Artacho, J. D. Gale, A. Garcia, J. Junquera, P. Ordejon, and D. Sanchez-Portal, "The SIESTA method for ab initio order-N materials simulation," J. Phys. Condens. Matter **14**, 2745–2779 (2002).

29. J. P. Perdew, K. Burke, and M. Ernzerhof, "Generalized gradient approximation made simple," Phys. Rev. Lett. **77**, 3865–3868 (1996).

30. N. Troullier and J. L. Martins, "Efficient pseudopotentials for plane-wave calculations," Phys. Rev. B **43**, 1993–2006 (1991).